

A Task-related and Resting State Realistic fMRI Simulator for fMRI Data Validation

Jason E. Hill^a, Xiangyu Liu, Brian Nutter, Sunanda Mitra*

^a Dept. of Electrical and Computer Engineering, Texas Tech University, Box 43102
Lubbock, TX USA 79409-3102

ABSTRACT

After more than 25 years of published functional magnetic resonance imaging (fMRI) studies, careful scrutiny reveals that most of the reported results lack fully decisive validation. The complex nature of fMRI data generation and acquisition results in unavoidable uncertainties in the true estimation and interpretation of both task-related activation maps and resting state functional connectivity networks, despite the use of various statistical data analysis methodologies. The goal of developing the proposed STANCE (Spontaneous and Task-related Activation of Neuronally Correlated Events) simulator is to generate realistic task-related and/or resting-state 4D blood oxygenation level dependent (BOLD) signals, given the experimental paradigm and scan protocol, by using digital phantoms of twenty normal brains available from BrainWeb (<http://brainweb.bic.mni.mcgill.ca/brainweb/>). The proposed simulator will include estimated system and modelled physiological noise as well as motion to serve as a reference to measured brain activities. In its current form, STANCE is a MATLAB toolbox with command line functions serving as an open-source add-on to SPM8 (<http://www.fil.ion.ucl.ac.uk/spm/software/spm8/>). The STANCE simulator has been designed in a modular framework so that the hemodynamic response (HR) and various noise models can be iteratively improved to include evolving knowledge about such models.

Keywords: Simulation; modeled ground-truth; fMRI; resting state fMRI; correlation; hemodynamic response; physiological noise.

1. INTRODUCTION

Various fMRI studies that require validation lack a comprehensive fMRI simulator¹. Despite the development of several fMRI simulators²⁻⁶ that generate fMRI data under various MRI system and signal models, no common data generation process is available, not only because of the lack of a common platform, but more importantly due to the challenges involved in modeling the HR variability⁷ and the various sources of motion and noise⁸⁻¹³. Historically, fMRI studies investigated simple activation maps that represent the average level of engagement in response to a specific stimulus or task¹⁴. The statistical fidelity of the claimed false-positive rates of the activation maps found by certain wide-spread fMRI analysis techniques have been questioned^{15,16}, and even the true-positive rates are unknown in task-based studies due to the lack of ground truth. Moreover, fMRI data analysis has progressed to a greater depth to reveal the neuronal organization of the human brain while performing a task, under the condition of exposure to a specific stimulus or even without stimulus, i.e. under the so called resting state fMRI (rs-fMRI)¹⁷⁻¹⁹. We propose to develop STANCE at multiple levels to serve as a validation tool for current research studies in fMRI focusing on the possibility of estimating and removing motion and physiological noise²⁰⁻²³. Future developments will be used to investigate the effect of noise and possible dynamics on resting-state/task-related time series and the corresponding estimation of the characteristic functional connectivity networks. STANCE will be able to estimate true- and false-positive rates from user-defined synthetic activation maps, as well as be able to simulate more sophisticated multi-task studies even with periods of rest²⁴.

2. METHODOLOGY

The organizational file structure of the simulator has three levels: study, subject, and session. Fig. 1 provides a flowchart illustrating the generation of a single fMRI volume. The first step is to create the fMRI study, which involves specifying the fMRI scanning protocol, loading or defining any neuronal activations being investigated, and specifying the

*sunanda.mitra@ttu.edu; phone 1 806 834-8074 x 242; fax 1 806 742-1245

experimental design and noise model. The next step is to select a subject from one of the 20 normal brain phantoms^{25,26} available in the simulated brain database BrainWeb. Each brain phantom has an anatomical volume and high resolution fuzzy membership volumes for 12 different tissue types, which are used in simulation. The third step is to allow specific factors of the session to be added, e.g. motion. Then, from the fMRI scan protocol and the brain phantom resources, the subject's "native space" is resliced to construct the "functional space," which is then used in the generation of a sequence of fMRI volumes from the EPI signal equation³¹.

2.1 Select the Subject Brain from among Twenty Normal Phantoms provided by BrainWEB

The subject brain is selected from the set of the 20 normal brain phantoms provided by BrainWEB. These phantoms are

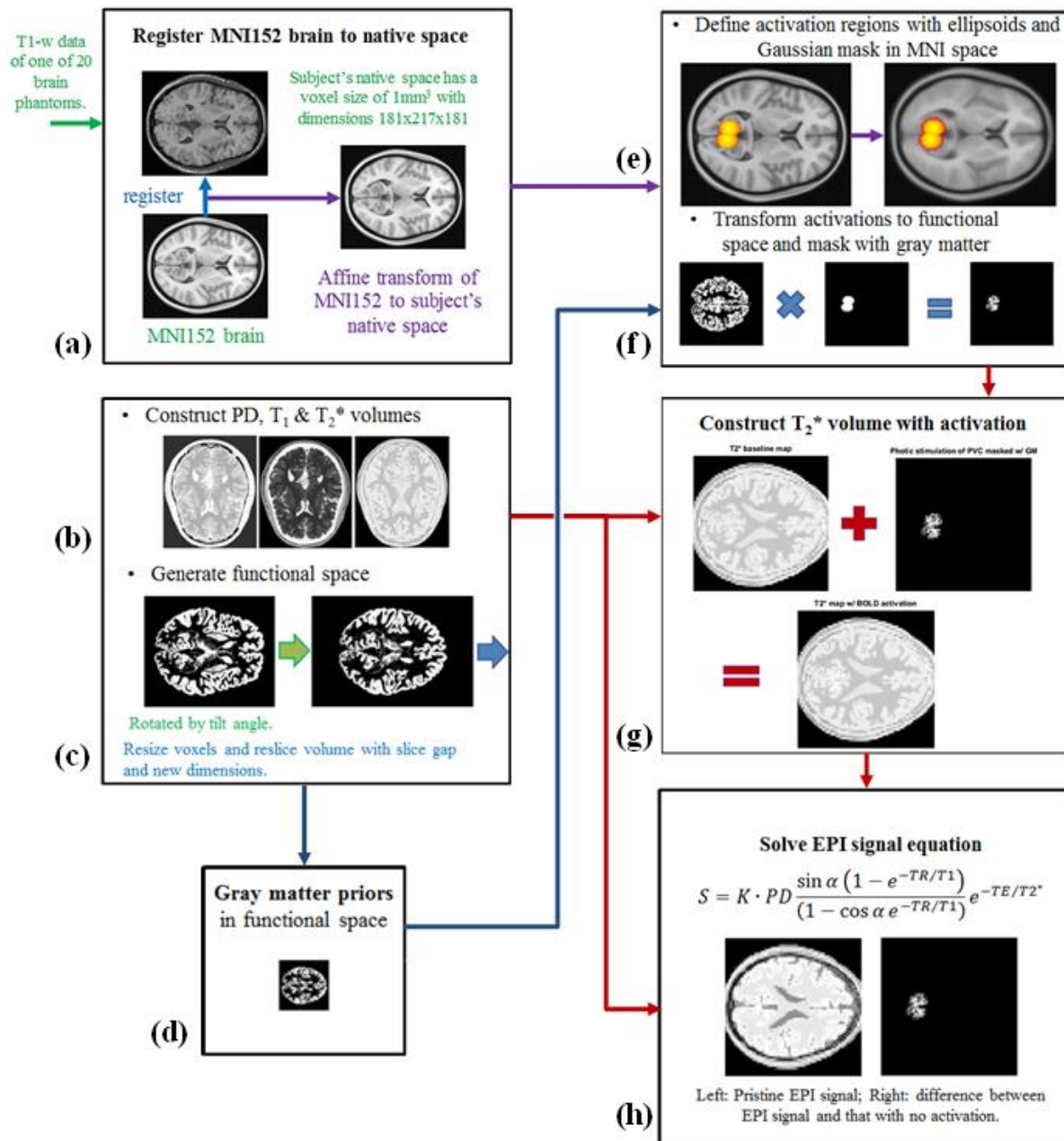


Figure 1. A Flowchart outlining the generation of an fMRI volume by STANCE.

derived from actual repeated head scans of 10 males and 10 females (ages 25-37); spatially transformed to set the anterior commissure (AC) as the origin and the AC-posterior commissure (PC) line to conform to MNI space^{25,26}. For each phantom, BrainWEB provides a noisy T1-weighted (T1-w) anatomical volume (1mm³ isotropic) and high resolution fuzzy membership volumes of 12 tissue types (0.5 mm³ isotropic) (see Figs. 2 and 3 in Ref. [26]). The priors for the gray matter (GM), white matter (WM), cerebrospinal fluid (CSF) and blood vessels (BV) are particularly useful in simulating various time-series in the brain. The 12 different tissue types have tabulated average values for proton density (PD), MR relaxation times (T1, T2, T2*) and chemical shift (δ), which can be used to estimate the variation of these parameters across the head in the subject's native space.

The provided T1-w anatomical volumes have a noise level of about 4% of peak signal intensity. Our first preprocessing step is to run them all through a bilateral filter. Next, following the procedure in Ref. [25] for all 20 brain phantoms, we use these filtered T1-w volumes to optimize the MR parameter averages by fitting them iteratively to the T1-w signal for the signal equation of the spin echo sequence.

The affine transformation matrix between the standard MNI152 brain and each subject brain is calculated once upon initialization and saved (see Fig. 1.a), which allows any resource (e.g. activation maps) defined in the Standard Stereotactic Space to be roughly transformable onto each phantom brain for simulation purposes (e.g. to rapidly transform of masks specified in MNI coordinates to a subject's native space). Additional affine transforms can be performed in order to increase subject variability.

Finally, the fuzzy membership volumes are resliced according to the fMRI scan parameters to a functional space, which is laid out with a user-specified voxel size, slice gap, inter-voxel spacing, and desired pitch tilt angle relative to the AC-PC line. The default setting has a 64×64 slice grid, isotropic fMRI voxel size of 3×3×3 mm³, a slice gap of 20% and a tilt angle of 15° to increase the signal above the nasal cavities (see Fig. 1.c-d. for the GM priors). The procedure is carried out by first applying an affine transformation to achieve rotation and Z-reslicing. Next, STANCE reslices to the functional space for all 12 tissue types. By default, the number of Z slices is automatically determined to span the GM given the requested protocol, although this too can be specified by the user.

2.2 Create PD, T1 and T2* Baseline Volumes

The fuzzy membership volumes of the 12 tissue types resliced to functional space, plus the average PD, T1 and T2* values for each tissue, are used to construct the PD, T1 and T2* baseline volumes for the subject (see Fig. 1.b). Except for motion, the T1 parameter volume is treated as static for the simulation. PD can also vary due to blood or CSF flow and pulsations. The T2* parameter volume in functional space is used as the baseline to add any further BOLD activations or fluctuations. Hence, these values can be used to generate desired fMRI data at any time point, such as the pristine signal that is assumed to represent the ideal, noiseless and artefact-free signal (see Fig. 1.g). These **parameter** volumes can be used to model almost any static MRI signal. This simulation is performed on demand for volumes in functional space, because its generation depends on the study-specific fMRI protocol, the subject-specific brain phantom, the noise model, and the requested motion.

2.3 Define Neuronal Activation Templates

Each study requires the definition of neuronal activation templates in order to properly simulate neuronal activation. The activation templates are specified in terms of MNI152 coordinates in Standard Stereotactic Space, where the origin is at the AC and the Y-axis is taken along the line from the AC to a point near the PC. Such templates are preferable because they can be saved compactly (e.g. described using MNI space) and then defined explicitly to a given native or functional space whenever the need arises. Five methods are available to define neuronal activation templates in STANCE: (1) data-derived maps; (2) geometric shapes; (3) atlas or parcellation regions of interests (ROIs); (4) an explicit list of coordinates; (5) combinations of any of the previous four by fuzzy logic operations or masking.

The preferred means to estimate neuronal activation templates is directly from data or atlases, i.e. from 3D statistical parameter maps (SPMs) or from 4D volumes with spatial maps indexed by components (e.g. components derived from anatomical parcellations or Independent Component Analysis (ICA)). If the activation map of a task is not available for a study of interest, templates can be constructed from reported characteristics of the observed activation, such as activation center, volume and morphology. An activation template map can thus be built from multiple loaded data or shape masks, combining them together in a logical OR-like manner (e.g. see Fig. 1.e). All activation maps are 8-bit with maximum value normalized to unity, and the maximum percent amplitude variation must be specified (2% of signal is default). Finally, the activation map is transformed, resized and resliced to the subject's functional space by an affine

transformation as determined from the fMRI protocol, in the same manner used to create the baseline volumes. Finally, the functional activation map is masked with the GM priors to restrict neuronal activation to the subject's cortex (see Fig. 1.f), and further adjustments are made to ensure that the resulting activated gray matter volume fraction is equivalent to that specified in MNI space. This result is the modeled neuronal activation map for the task for that subject.

2.4 Specify BOLD Activation: Spatial Maps

BOLD-like changes to the fMRI signal have a TE dependence, which is encoded in T2* dynamics according to the signal equation in Fig. 1. Any desired activation map can be added to the T2* baseline volume based upon the assumed linear additive property of BOLD activation, which is justifiable as long as refractory effects are avoided under certain conditions^{27,28}. Next, the subject's activation map is mathematically adjusted to the percent change in T2* that would produce the specified maximum percentage of *signal* amplitude change based upon the fMRI scan protocol. From the EPI signal equation (Fig.1) we find that the relative change in T2* is related to the relative change in signal, *S*, by:

$$\% \Delta T2^* = \frac{\ln(1 + \% \Delta S)}{\frac{TE}{T2^*} - \ln(1 + \% \Delta S)} \approx \% \Delta S \frac{T2^*}{TE} \left[1 + \% \Delta S \left(\frac{T2^*}{TE} - \frac{1}{2} \right) \right]. \quad (1)$$

Thus for a TE = 50 ms, a 3% change in BOLD signal in the cortex corresponds to about a 4.25% relative change in the T2* value. Hence for larger TEs, these two quantities have comparable changes and can be manipulated in similar fashions. Finally, the constructed change in T2* due to the modelled activation is added to the baseline. The result is a snap-shot of a T2* volume that incorporates changes due to the activation's BOLD response (see Fig. 1.g). Some effects, like field inhomogeneities and BOLD-like effects are best handled with the T2* dynamics, while others, e.g. system noise, are better added to the signal or PD.

2.5 Specify BOLD Activation: Time-Series

Any fMRI simulator must simulate the fMRI data time-series, e.g. the BOLD signal from an ideal task-related activation is shown in Fig. 2. It should be noted that because the fMRI sequence images an entire slice at a time, the natural signal

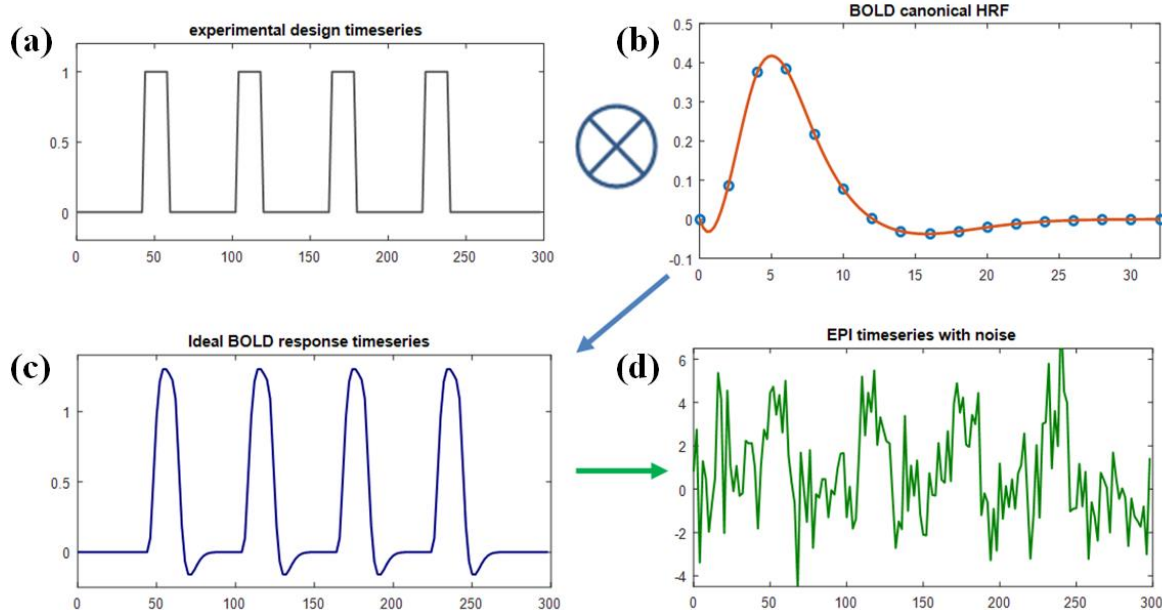


Figure 2. Simulation of task-related response of a voxel with peak activation: a). an experimental design time-series is convolved with b). the canonical BOLD hemodynamic response function (HRF) to yield c). the ideal expected BOLD response, used to generate the EPI signal. d). Noise with a magnitude on the order of the BOLD response is added to yield the synthetic EPI signal (its vertical axis is deviation from baseline, arbitrary units). Horizontal axes all are time (sec).

sample time is $\delta t = (TR/N_{\text{slices}}) \cdot (\text{Acceleration Factor})$, so all subsequent time-series will be simulated at this time resolution and then downsampled according to the slice timing to generate the resulting fMRI signal with time resolution TR. First, the experimental design time-series is required for all tasks in a study (e.g. see Fig. 2.a). This is the idealized stimulus/response time-series for task-evoked neuronal activation, although in practice no subject's on-task attentiveness is 100%, and realistic simulation must include this effect. Next, the task-evoked stimulus time-series is convolved with the hemodynamic response function (HRF) to yield the ideal expected BOLD response time-series (e.g. see Fig. 2.c.). A "generalized form" of the canonical HRF is defined as the sum of two Gamma distributions

$$h_{gc}(t; \tau, \zeta, c) = A e^{-t} \left[\frac{t^{\tau}}{\Gamma(\tau + 1)} - c \frac{t^{\zeta}}{\Gamma(\zeta + 1)} \right], \quad (2)$$

where t is in seconds, $\Gamma(z)$ is the gamma function, A is an arbitrary amplitude that can be determined from integration normalization $N = A(1 - c)$, $\tau > 0$ denotes the time to the first peak, $\zeta > \tau$ relates the time to the next valley floor after the first peak, and $c > 0$ controls the ratio $\rho(\tau, \zeta, c)$ of the valley and peak magnitudes. The canonical HRF (as generated by SPM) is normalized to $N = 2$ (so $A = 2.4$) and has $\tau = 5$, $\zeta = 15$, $c = 1/6$ (see Fig. 2.b). It is known that the HRF varies across a subject's brain and between subjects and certain populations^{7,13}. More realistic simulations will include maps of these "generalized canonical HRF" parameters to account for this variation.

2.6 Generate the EPI Signal

The simulation of the MR signal handles the pulse sequence's effects on the spin ensembles as discrete events. The state of tissue magnetization is tracked for every pulse sequence event, such as RF pulse, field gradient, and echo time²⁹. A simple phenomenological model of the tissue magnetization vector behavior is the Bloch equation³⁰, with parameters: M_0 , the equilibrium magnetization (proportional to PD); T_1 , the longitudinal relaxation time; T_2 , the transverse relaxation time. MR is useful for imaging because each tissue type generally has a different T_1 , T_2 and/or PD. Pulse sequences can be designed to enhance the signal for a particular tissue or enhance contrast between different tissue types.

From the fMRI scan protocol, pulse sequence, and the PD, T_1 , and BOLD-like T_2^* parameter maps in functional space, the Bloch equation can be solved for every voxel and time. The steady-state solution of the Bloch equation for a given pulse sequence results in the signal equation for that pulse sequence. We accomplish an accelerated simulation of the fMRI signal, S , for an Echo Planar Imaging-Gradient-Recalled Echo (EPI-GRE) sequence³¹, according to the T_1 , T_2^* , and PD parameter maps and the slice timing order of acquisitions, by using the EPI signal equation in Fig. 1, where K is a constant dependent on the magnetization, scanner and shimming, TR is the volume-wise repeat time (typically ranging from 0.3-3 s), TE is the echo time (typically 20-50 ms), and the flip angle (FA) can be small ($\alpha = 5-20^\circ$) to suppress the T_1 -weighting or large ($\alpha = 78-90^\circ$) to get more signal. Thus, at any echo time, the MRI signal can be estimated **and any location**. Note that the defining feature of fMRI simulators is in handling the fMRI time-series and that most do not solve the Bloch equation. Some simulators simply add activations and noise to a MR signal baseline, never considering the MRI parameters⁴⁻⁶. The ones that do handle a user-provided T_2^* time course and a pulse sequence as inputs to its Bloch simulator of the MR scanner require a significant time investment for larger group studies^{2,3}. We aim to make STANCE flexible yet fast, able to simulate both extremes, while making it into a tool that can prepare 4D PD, T_1 and T_2^* data for existing Bloch equation solvers as well as approximately reproducing such solutions in an accelerated fashion. The final output is a synthetic fMRI volume that is saved as a NIfTI file and can be analyzed with the same tools as real data, except that now the neuronal activation map is also available for benchmarking, e.g. quantification of true/false positive rates, or benchmarking denoising/motion correction techniques.

2.7 Add Noise, Attenuation and Motion

Various forms of noise can be modelled and linearly added to the signal according to the accepted total image noise model of the different noise components:

$$\sigma = \sqrt{\sigma_0^2 + \sigma_P^2} = \sqrt{\underbrace{\sigma_T^2 + \sigma_S^2}_{\sigma_0^2} + \underbrace{\sigma_B^2 + \sigma_{NB}^2}_{\sigma_P^2}}, \quad (3)$$

where σ_0 is the raw system noise (see Fig. 3.a), which can be further decomposed into thermal noise, σ_T , and other system noise σ_S , which is due to low frequency drift and field inhomogeneities from the MR scanner; and σ_P is the

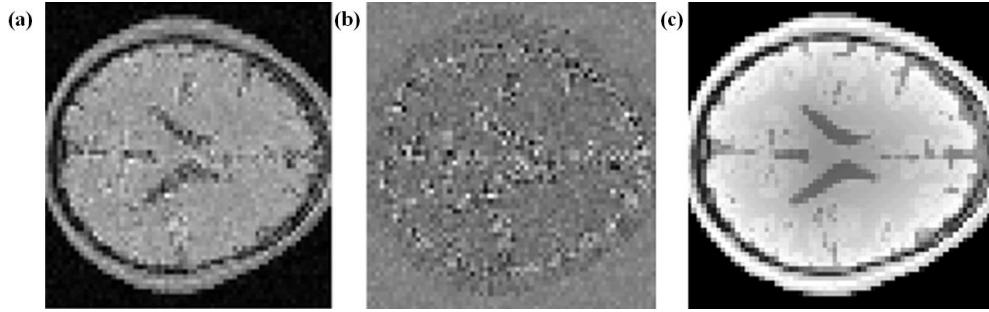


Figure 3. Synthetic results: (a) with 4% of peak system noise in GM (and double of that in CSF and blood vessels); (b) difference between noisy and pristine signals; (c) an attenuated signal (exponential fall-out parameter: $\lambda = 8.33$ mm).

physiological noise, which can be separated into BOLD-like noise, σ_B , which is metabolically-linked, and non-BOLD-like noise, σ_{NB} , which are dependent on and independent of TE, respectively⁸. The BOLD signal registers changes in blood oxygenation level, flow and volume³², and it is important to separate out sources due to neuronal activation via neurovascular coupling from physiological confounds³³.

Drift can be modeled as very low frequency polynomials or sinusoids. In the absence of other factors a measured MR signal, S_M , arises from adding complex noise, σ_0 , to the complex MR intrinsic signal, S_A , i.e. $S_M = S_A + \sigma_0 [N(0, 1) + jN(0, 1)]$, where $N(0, 1)$ denotes a normal distribution of zero mean with unit variance, and j is the square root of -1, which causes MRIs to exhibit noise with a Rician distribution³⁴. Time invariant noise can be modeled simply as Rician noise that can vary across the brain (see Fig. 2.d.), while the time dependence of other noise sources must be handled further.

Noise that arises from the scanner is independent of signal strength, while physiological noise increases linearly with signal strength according to Krüger and Glover's model⁸, $\sigma_P = \lambda \langle S(t) \rangle$, where the achievable temporal signal to noise (tSNR) at high signal strengths and field strengths, relative to $\text{tSNR}_0 = \langle S(t) \rangle / \sigma_0$, is asymptotic to

$$\text{tSNR} = \frac{\text{tSNR}_0}{\sqrt{1 + \lambda^2 \text{tSNR}_0^2}}. \quad (4)$$

Higher frequency physiological noise comes from six main sources¹¹⁻¹³: (1) respiratory pulse (RP), which follows the respiratory lung volume time-series, $\text{RVT}(t)$; (2) cardiac pulse (CP), which follows the blood flow pulse wave velocity time-series, $\text{PWV}(t)$, that is modulated by the heartbeat, $\text{HB}(t)$; (3) interaction between cardiac and respiratory phases (InterCRP), which approximately follows the product of RP and CP time-series; (4) respiratory volume (RV) response, which comes from convolving the respiratory response function (RRF) with the $\text{RVT}(t)$; (5) heart rate (HR) response, which comes from convolving the cardiac response function (CRF) with the $\text{HRV}(t)$; (6) arterial blood pressure $\text{ABP}(t)$, described by Mayer waves with a frequency ~ 0.1 Hz inducing a fluctuation about $\sim 25\%$ of that caused by HR³⁵. The first three sources are partially filtered out by Retrospective Image Space Correction of Physiological Noise (RETROICOR), its developments and rivals³⁶⁻³⁹; however, each of these methods still leaves low frequency physiological noise in the data. Very low frequency components, like CSF flow, will often get processed out with drift, and care must also be taken to separate out the variability due to spontaneous activation in the cortex and noise that can have similar BOLD-like or spectral properties^{22,23,40,41}. This remains an open problem^{9,10}.

First, we simulate the impulse series of the respiratory cycle, with the default respiration interval (RI) set at 4.0 s and its variance at 0.25 s⁴². The vertical displacement of the chest during regular respiration is then modeled for the i^{th} cycle as

$$d(\varphi_i) = A_i \cos^4(\pi \varphi_i), \quad (5)$$

where $\varphi \in [-0.5, +0.5]$ parametrizes the time/RI, relative to the i^{th} impulse⁴³, and the amplitude A_i is proportional to the RI with default average of 1.0 cm (see red curve in Fig. 4.a). From the chest motion time series $\Delta r(t) = 0.58 \cdot d(t)$, an ellipsoid model of the lungs is used to yield the respiratory lung volume:

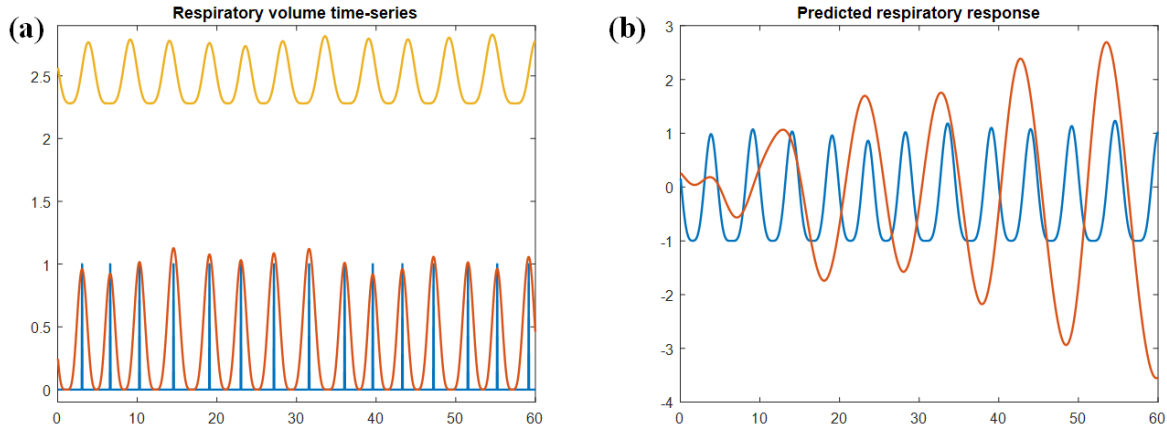


Figure 4. Respiratory-related time-series. a). respiratory impulse (blue), chest displacement from Eq. (5) added to the impulses with vertical units of cm (red), and the respiratory lung volume time-series $RVT(t)$ for a 75 kg subject from Eq. (6) with vertical units of L (yellow). b). the quasi-sinusoidal $RVT(t)$ (blue) used to modulate heart rate, and the predicted respiratory response derived from a convolution with the RRF of Eq. (7) given $\sigma^2 = 1$. Horizontal axes are all time (s).

$$RVT(t) = \frac{4\pi W}{300 kg} [11 cm + \Delta r(t)] [11 cm + \Delta r(t)] [6 cm + \Delta r(t)], \quad (6)$$

which yields typical lung exhalation and inhalation volumes according to established norms^{44,45} (see yellow curve in Fig. 4.a). The normalized baseline form of $RVT(t)$ is used as the basis of the respiratory pulse time-series $RP(t)$.

Just as the HRF is a sum of two gamma distributions, the average RRF for healthy adults has been modelled as

$$RRF(t) = 5.661 \frac{t^{2.1} e^{-t/1.6}}{\Gamma(3.1) 1.6^{3.1}} - 20.159 \frac{t^{3.54} e^{-t/4.25}}{\Gamma(4.54) 4.25^{4.54}}, \quad (7)$$

which is convolved with the $RVT(t)$ to produce a response that is observed to induce low-frequency (<0.1 Hz) signal fluctuations on the fMRI signal^{20,46} (see the red curve of Fig. 4.b).

With the cardiac signal, the generalized integral pulse frequency modulation model (IPFM) is a well-established model of heart rate variability (HRV)⁴⁷; it imposes a threshold on the integral containing the modulating signal:

$$m(t) = \sum_n a_n f_n(\omega_n t + \phi_n), \quad (8)$$

where ω_n and ϕ_n are the component frequency and phase shift for the n^{th} component, respectively, and f is a quasi-periodic function, taken to be a cosine in the traditional model. The instantaneous heart rate is then given by $(1 + m(t))/T$, where T is the average time period between beats. Analysis of HRV data for healthy subjects in a supine position yields a set of three almost equally weighted spectral bands at $\omega_1 = 0.01$ -0.03, $\omega_2 = 0.09$ -0.11 and $\omega_3 = 0.2$ -0.3 Hz, denoted as very low frequency (VLF), low frequency (LF) and high frequency (HF), respectively⁴⁸. The HF frequency band is called the Respiratory Sinus Arrhythmia (RSA), which suggests the use of a quasi-sinusoidal form of $RVT(t + \phi_3)$, for the modulation function⁴⁹. The LF frequency band is due to Mayer waves, while the VLF is thought to be due to environmental or vascular mechanisms or both⁵⁰. The quasi-periodic functions for the LF and VLF bands can be generated using an exponent of 2 instead of 4 in Eq. (5), thus allowing synthesized HRV(t) and HB(t) time-series, (see Fig. 5.a). The average CRF has been empirically fit to a sum of a Gamma distribution and a Gaussian distribution:

$$CRF(t) = 14.243 \frac{t^{2.7} e^{-t/1.6}}{\Gamma(3.7) 1.6^{3.7}} - \frac{16}{3\sqrt{2\pi}} \exp\left[-\frac{(t-12)^2}{18}\right] \frac{t^{3.54} e^{-t/4.25}}{\Gamma(4.54) 4.25^{4.54}}, \quad (9)$$

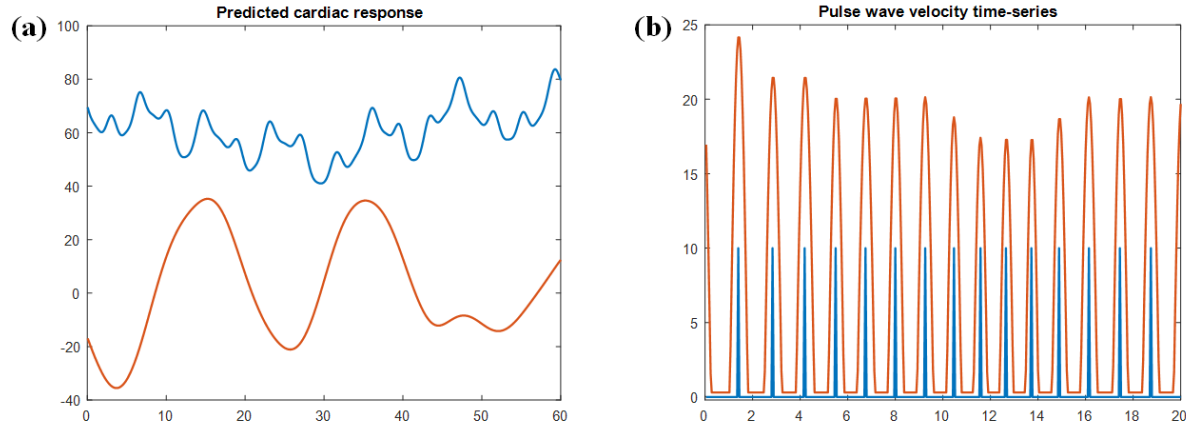


Figure 5. Cardiac-related time-series. a). heart rate variability time-series, $HRV(t)$ from a generalized IPFM using physiological signals in Eq. (10) in units of beats/min (blue), and the corresponding cardiac response (red) with $\sigma^2 = 20$ for display purposes. b). the impulse cardiac heart beat time-series (blue), and the pulse wave velocity time-series $PWT(t)$ with units of mm/s (red). Horizontal axes are all time (s).

which is convolved with $HRV(t)$ to produce the hemodynamic response due to change in heart rate²¹ (see Fig. 5.b).

The cardiovascular PWV can be synthesized in a fashion similar to the procedure as detailed above for Eq. (5), where the arterial velocity of the blood is simply modeled, from observations in the radial artery, for the i^{th} cardiac cycle as

$$v(\theta_i) = 0.1v_0 + 1.8\pi v_0 T_i |\cos(2\pi \theta_i T_i + \psi)|, \quad (10)$$

where $\theta \in [-0.25, +0.25]$ parametrizes the times, a quarter of a cycle before and after the i^{th} heartbeat, v_0 is the average blood velocity, and ψ is a cardiac phase offset that can vary spatially^{51,52}. We model the average blood velocity in a voxel as $v_0 = 3 + 200\rho_{BV}$ mm/s based on known velocities^{52,53}. Finally, the InterCRP can be generated from the product of $RVT(t)$ and $PWV(t)$ ²⁶. The extent of the role that physiological noise plays as the source of the observed correlation in fMRI time-series remains an open problem¹³. The six time-series are combined according to observed contributions to the signal variance¹², $\sigma_{P,m} = \lambda_m \langle S(t) \rangle$, and added to the signal according to Eq. (4), according to tissue type m ⁸.

In addition, signal attenuation due to coil effects can be modeled (see Fig. 3.c). This sometimes occurs at higher field strengths or when parallel/accelerated imaging uses other coils in addition to the head coil. Such attenuation has a signal fall-off that trends as $\exp(-\lambda \Delta r)$ where Δr is the shortest distance to the edge of the head.

3. RESULTS

3.1 Photoc Stimulation of the Visual Cortex

In the example shown in Fig. 1, a model of photic stimulated activation of the visual cortex is defined by two ellipsoids with centers $[7, -68, 8]$ and $[-8, -65, 8]$ (MNI coordinates); both with the estimated volume 5,000 mm³, an aspect ratio of 4:3:4, and rotations from the X-axis of -30° and $+30^\circ$ respectively and 0.005 exponential fall-off with a floor (min amplitude) of 0.2 of maximum. This is a synthetic model of the activation observed in the very first fMRI experiment published in 1991⁵⁴. Noise, attenuation and artefacts can be added to the pristine EPI signal as shown in Fig. 3. The final result is stored in a compressed NIFTI file format.

3.2 Right-Handed Finger-Related Task

The estimated activation template of a right-handed finger-related task is shown in the top row of Fig. 6. This template was generated from data available on Neurosynth (<http://www.neurosynth.org>). They provide both forward inference and reverse inference statistical maps derived from a meta-analysis of 60 studies mentioning the term “finger tapping.” The two maps were combined via a fuzzy logical AND operation after applying a minimum t -statistic threshold of $t = 5.0$. Finally, in the resulting mask, to simulate right-hand only activation, any activation in the right hemisphere was reflected on to the left side of the brain. The activation template and resulting BOLD-related activation map in a subject

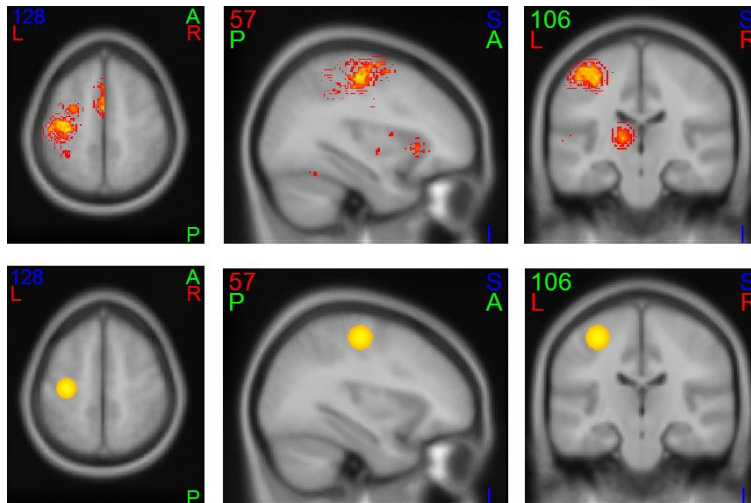


Figure 6. Task-evoked neural activation example. Top row: the orthographic view of activation due to a right-handed finger-related tasks, derived from meta-analysis data ($t > 5.0$) of 60 studies available on Neurosynth. Bottom row: the same orthographic view of the finger opposition task activation template as modeled in MNI space from reported values⁵⁵. Right: axial slice with largest activation. Middle: the sagittal slice on the left side with the largest activation. Left: coronal slice with the largest activation. Colors label the directions according to the convention in diffusion tensor imaging.



Figure 7. The orthographic view of the BOLD-related activation map in functional space, constructed from a transformation of the activation template and masking with the GM priors, for the right-handed finger-related task shown in Figure 6: (a) truncated axial, (b) sagittal, (c) coronal, and (d) resulting axial slice of EPI signal with rigid-body motion.

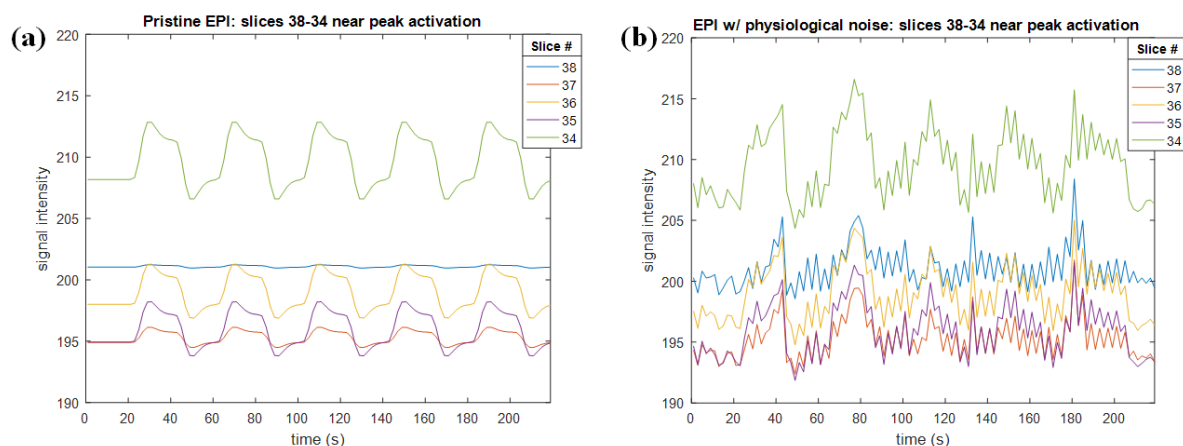


Figure 8. Resulting synthetic EPI-signal time-series. a). pristine noiseless signal from expected BOLD response and perfect subject on-task engagement with periods of rest and finger task alternating in 20 sec block. b). the same with physiological noise added by generating times-series according to Eqs. (3-10). No lag times have been added so temporal variations in the noise time-series between slices are solely due to slice-timing. Peak activation is at [20, 32, 34].

for a finger-related task is shown in Figs. 6 and 7, respectively. The generation of synthetic fMRI data for this task, both ideal and with the addition of physiological noise, has also been accomplished (see Fig. 8).

4. CONCLUSION

A realistic fMRI simulator called STANCE that allows user-defined activations and modular improvements has been initiated, with the goal to include not only task-related time-series as directed by an experimental design⁵⁶ convolved with a spatially varying HRF⁷, but also to include resting state time-series driven by a potentially dynamic correlation matrix¹⁹. STANCE can serve as a benchmark for various fMRI analyses via statistical error quantification from activation maps and be used as an educational tool for beginners interested in learning about fMRI studies.

ACKNOWLEDGEMENTS

This work has been supported by the NLM-NIH contract [HHSN276201 500690P]. We gratefully acknowledge many discussions, evaluations & feedback regarding this research effort with Oliver Xie, L. Rodney Long, & Sameer Antani.

REFERENCES

- [1] Welvaert, M. and Rosseel, Y., "A review of fMRI simulation studies," PLoS ONE 9(7): e101953 (2014).
- [2] Drobnjak, I., "fMRI simulator: Development and Applications," Ph.D. Thesis, University of Oxford (2007).
- [3] Ning, X., Fitzpatrick, J. M., Yong, L., Dawant, B. M., Pickens, D. R., and Morgan, V. L., "Computer-generated fMRI phantoms with motion-distortion interaction," Magn. Reson. Imag., 25, 1376-1384, (2007).
- [4] Welvaert, M., Durnez, J., Moerkerke, B., Verdoolaege, G., and Rosseel, Y., "neuRosim: An R package for generating fMRI data," J. Stat. Software 044(i10) online (2011).
- [5] Friston, K., Moran, R. and Seth, A. K. "Analysing connectivity with Granger causality and dynamic causal modelling," Current Opinions in Neurobiology 23(2), 172-178 (2013).
- [6] Allen, E., Erhardt, E., Wei, Y., Etchele, T., and Calhoun, V., "A simulation toolbox for fMRI data: SimTB," online user manual, available at <http://mialab.mrn.org>.
- [7] Handwerker, D. A., Gonzalez-Castillo, J., D'Esposito, M., and Bandettini, P. A., "The continuing challenge of understanding and modeling hemodynamic variation in fMRI" NeuroImage 62(2), 1017-1023 (2012).
- [8] Krüger, G. and Glover, G. H., "Physiological Noise in Oxygenation-Sensitive Magnetic Resonance Imaging," Magn. Reson. Med. 46, 631-637 (2001).
- [9] Bright, M. G., and Murphy, K. "Removing motion and physiological artifacts from intrinsic BOLD fluctuations using short echo data," NeuroImage 64, 526-537 (2013).
- [10] Bright, M. G., and Murphy, K. "Is fMRI 'noise' really noise? Resting state nuisance regressors remove variance with network structure," NeuroImage 114, 158-169 (2015).
- [11] Nunes, S., "Characterization of physiological noise in resting-state fMRI data at 7T", Thesis, Técnico Lisboa (2014).
- [12] Wu, G-R., and Marinazzo, D., "Hemodynamic response function in resting brain: disambiguating neural events and autonomic effects" bioRxiv (beta): the preprint server for biology, doi: <https://doi.org/10.1101/028514> (2015).
- [13] Wu, G-R., and Marinazzo, D., "Sensitivity of the resting state hemodynamic response function estimation to autonomic nervous system fluctuations" Phil. Trans. R. Soc. A., in press (2017).
- [14] Rogers, B. P., Morgan, V. L., Newton, A. T., and Gore, J. C. "Assessing functional connectivity in the human brain by fMRI," Magn. Reson. Imag. 25, 1347-1357 (2007).
- [15] Eklund, A., Nichols, T. E. and Knutsson H., "Cluster failure: Why fMRI inferences for spatial extent have inflated false-positive rates," Proc. National Academy for Sciences USA, 109(28), 5487-5492 (2012).
- [16] Gonzalez-Castillo, J. Saad, Z. S., Handwerker, D. A., Inati, S. J., Brenowitz, N. and Bandettini, P. A. "Whole-brain, time-locked activation with simple tasks revealed using massive averaging and model-free analysis," Proc. National Academy for Sciences USA 113(28), 7900-7905 (2016).
- [17] Biswal, B., DeYoe, E. A., and Hyde, J.S. "Reduction of Physiological Fluctuations in fMRI Using Digital Filters," Magn. Reson. Med. 35(1), 107-113, (1996).
- [18] Bandettini, P. A., "Functional MRI Limitations and Aspirations," chap. in [Neural Correlates of Thinking], Kraft, E., Gulyás, B., Pöppel, E. (Eds.), Vol. 1 of the series On Thinking, Springer-Verlag, Berlin, 15-38, (2009).

- [19] Hutchison, R. M., Womelsdorf, T., Allen, E.A., Bandettini, P.A., Calhoun, V.D., Corbetta, M., Della Penna, S., Duyn, J. H., Glover, G. H., Gonzalez-Castillo, J., Handwerker, D. A., Keilholz, S., Kiviniemi, V., Leopold, D.A., de Pasquale, F., Sporns, O., Walter, M., and Chang, C., "Dynamic functional connectivity: Promise, issues, and interpretations," *NeuroImage* 80, 360-378, (2013).
- [20] Birn, M. B., Smith, M. A., Jones, T. B., and Bandettini, P. A. "The respiration response function: The temporal dynamics of fMRI signal fluctuations related to changes in respiration," *NeuroImage* 40(2), 644–654 (2008).
- [21] Chang, C., Cunningham, J. P., and Glover, G. H., "Influence of heart rate on the BOLD signal: The cardiac response function", *NeuroImage* 44, 857–869 (2009).
- [22] Kundu, P., Inati, S.J., Evans, J.W., Luh, W.M., and Bandettini, P.A., "Differentiating BOLD and non-BOLD signals in fMRI time series using multi-echo EPI," *NeuroImage* 60(3), 1759-1770 (2012).
- [23] Lombardo, M. V., Auyeung, B., Holt, R. J., Waldman, J., Ruigrok, A. N. V., Mooney, N., Bullmore, E. T. Baron-Cohen, S., and Kundu, P., "Improving effect size estimation and statistical power with multi-echo fMRI and its impact on understanding the neural systems supporting mentalizing," *NeuroImage*, 142, 55-66 (2016).
- [24] Gonzalez-Castillo, J., Hoya, C. W., Handwerker, D. A., Robinson, M. E., Buchanan, L. C., Saad, Z. S. and Bandettini, P. A. "Tracking ongoing cognition in individuals using brief, whole-brain functional connectivity patterns" *Proc. National Academy of Sciences USA* 112 (28), 8762–8767 (2016).
- [25] Aubert-Broche, B., Evans, A. C. and Collins, L., "A new improved version of realistic brain phantoms," *NeuroImage* 32, 138–145 (June 2006).
- [26] Aubert-Broche, B., Griffin, M., Pike, G. B., Evans, A. C. and Collins, D. L. "Twenty New Digital Brain Phantoms for Creation of Validation Image Data Bases," *IEEE Trans. on Med. Imaging* 25 (11), 1410–1416 (Nov. 2006).
- [27] Boynton, G. M., Engel, S. A., Glover, G. H., and Heeger, D. J., "Linear systems analysis of functional magnetic resonance imaging in human V1," *J. Neurosci.* 16(13), 4207-21 (1996).
- [28] Dale, A. M., and Buckner, R. L., "Selective averaging of rapidly presented individual trials using fMRI," *Hum. Brain Mapp.* 5(5), 329-40 (1997).
- [29] Kwan, R., Evans, A. C., and Pike, G. B., "An extensible MRI simulator for post-processing evaluation," *BrainWeb: Simulated Brain Database*, <http://www.bic.mni.mcgill.ca/brainweb/>.
- [30] Bloch, F. "Nuclear Induction," *Phys. Rev.* 70(1), 460-474 (1946).
- [31] Liang, Z-P., and Lauterbur, P. C., [Principles of Magnetic Resonance Imaging: A Signal Processing Perspective], Wiley-IEEE Press, New York, Eq. (9.24), 299 (1999).
- [32] Ogawa, S., Lee, T. M., Kay, A. R. and Tank, D.W. "Brain magnetic resonance imaging with contrast dependent on blood oxygenation," *Proc. Natl. Acad. Sci. USA* 87(24), 9868-9872 (1990).
- [33] Birn, R. M. "The role of physiological noise in resting-state functional connectivity," *NeuroImage* 62(2), 864-870 (2012).
- [34] Gudbjartsson, H. and Patz, S., "The Rician Distribution of Noisy MRI Data," *Magn. Reson. Med.* 34(6), 910–914 (1995).
- [35] Katura, T., Tanaka, N., Obata, A., Sato, H., and Makia, A., "Quantitative evaluation of interrelations between spontaneous low frequency oscillations in cerebral hemodynamics and systemic cardiovascular dynamics," *NeuroImage* 31(4), 1592-1600 (2006).
- [36] Glover, G. H., Li, T. Q. and Ress, D. "Image-based method for retrospective correction of physiological motion effects in fMRI: RETROICOR," *Magn. Reson. Med.* 44(1), 162-167 (2000).
- [37] Law, C.S. Liu, C., and Glover, G.H. "Sliding Window SENSE Calibration for Reducing Noise in fMRI," *Magn. Reson. Med.* 60(5), 1090-103 (2008).
- [38] Särkkä S., Solin, A., Nummenmaa, A., Vehtari, A., Auranen, T., Vanni, S., and Lin, F.H., "Dynamic Retrospective Filtering of Physiological Noise in BOLD fMRI: DRIFTER," *NeuroImage* 60(2), 1517–1527 (2012).
- [39] Kasper, L., "Physiological Noise Correction – an Introduction to PhysIO Toolbox", MR-Technology Group & Translational Neuromodeling Unit, University of Zurich (2015).
- [40] Niazy, R. K., Xie, J., Miller, K., Beckmann, C. F., and Smith, S.M., "Spectral characteristics of resting state networks," *Prog. Brain Res.*, E. J. W. Van Someren et al. (Eds.), 193(1), 259-276 (2011).
- [41] Evans, J. W., Kundu, P., Horovitz, S. G., and Bandettini, P.A. "Separating slow BOLD from non-BOLD baseline drifts using multi-echo fMRI," *NeuroImage*, 105, 189-197 (2015).
- [42] Barrett, K. E., Barman, S. M. Boitano, S. and Brooks H., [Ganong's Review of Medical Physiology] (24th ed.), McGraw-Hill, New York, 619 (2012).
- [43] Lujan, A. E., Balter, J. M. and Ten Haken, R. K., "A method for incorporating organ motion due to breathing into 3D dose calculations in the liver: sensitivity to variations in motion," *Med. Phys.* 30(1), 2643–2649 (2003).

- [44] A. Delawari and R. Doelman, "Simulation of an Artificial Respiratory System: Choosing a New Actuator for Implementation in a Lung Simulator," B.Sc. Thesis, The University of Delft (2010).
- [45] Jones R. L. and Nzekwu, M. M., "The effects of body mass index on lung volumes," *Chest*. 30(3), 827–33 (2006).
- [46] Cordes, D., Nandy, R. R., Schafer, S., and Wage, T. D., "Characterization and Reduction of Cardiac- and Respiratory-Induced Noise as a Function of the Sampling Rate (TR) in fMRI" *NeuroImage* 89, 314-30 (2014).
- [47] Bayly, E. J., "Spectral analysis of pulse frequency modulation in the nervous systems," *IEEE Trans. Biomed. Eng.*, BME 15(1) 257–265, (1968).
- [48] I. P. Mitov, "Spectral analysis of heart rate variability using the integral pulse frequency modulation model" *Med. Biol. Eng. Comput.* 39(1), 1-7 (2001).
- [49] Meste, O., Blain, G., and Bermon, S., "Some Considerations on the IPFM Model for the Heart Rate Variability Analysis" *Computers in Cardiol.* 30, 709–712 (2003).
- [50] Attarodi, G., Dabanloo, N. J., Abbasvandi, Z., and Hemmat, N., "A New IPFM Based Model For Artificial Generating Of HRV With Random Input," *Int. J. Comp. Sci. Issues*, 10(2), 1-5 (2013).
- [51] Zambanini, A., Cunningham, S. L., Parker, K. H., Khir, A. W., Thom, S. A. and Hughes, M. A. D., "Wave-energy patterns in carotid, brachial, and radial arteries: a noninvasive approach using wave-intensity analysis" *Am. J. Physio. - Heart & Circulatory Physio.* 289(1), H270-H276 (2005).
- [52] Arimon, J. A., "Numerical modelling of pulse wave propagation in the cardiovascular system: development, validation and clinical applications" Ph.D. Thesis, The University of London (2006).
- [53] Rengachary, S. S. and Ellenbogen, R. G., (Eds.), [Principles of Neurosurgery], Elsevier Mosby, Edinburgh (2005).
- [54] Belliveau, J. W., Kennedy, D. N., McKinstry, R. C., Buchbinder, B. R., Weisskeopf, R. M., Cohen, M. S., Vevea, J. M., Brady, T. J. and Rosen, B. R. "Functional Mapping of the Human Visual Cortex by Magnetic Resonance Imaging," *Science* 254(5032), 716-9 (1991).
- [55] Ramsey, N. F., Kirkby, B. S., Van Gelderen, P., Berman, K. F., Duyn, J. H., Frank, J. A., Mattay, V. S., Van Horn, J. D., Esposito, G., Moonen, C. T. W., and Weinberger, D. R., "Functional Mapping of Human Sensorimotor Cortex with 3D BOLD fMRI Correlates Highly With H₂¹⁵O PET rCBF," *J. Cereb. Blood Flow Metab.*, 16, 755-764, (1996).
- [56] Bandettini, P. A., Wong, E. C., Tikofsky, R. S., Hinks, R. S., and Hyde, J. S., "Time course EPI of human brain function during task activation," *Magn. Reson. Med.* 25, 390-397 (1992).